

Chapter 4

Timing and Spectral properties of Accreting Milli-second X-ray Pulsar Swift J1756.9-2508

4.1 Introduction

Swift J1756.9-2508 is a 5.5 ms accreting milli-second X-ray pulsar (AMXP) discovered in 2007 (Krimm *et al.* (2007a); Markwardt *et al.* (2007)). The companion of the neutron star in Swift J1756.9-2508 is a He-dominated brown dwarf and has an orbital period of 54.7 min (Krimm *et al.*, 2007b). The estimated magnetic field of the source is about 3.1×10^8 G (Sanna *et al.*, 2018). Bult *et al.* (2018) has done correction on the source coordinates through an astrometric analysis of the arrival time of pulse. The corrected coordinates are R.A. = $17^h 56^m 57.18^s \pm 0.08^s$ and Dec. = $-25^\circ 0' 27.8'' \pm 3.5''$.

A part of the chapter of the thesis is published in *Mon. Not. Roy. Astron. Soc.* 489, 5858-5865 (2019)

The timing and spectral analysis of the pulsar Swift J1756.9-2508 are carried out in detail in this chapter. The source spectrum in a broad 0.3-79 keV energy range are fitted with theoretical models. A detail analysis of the pulse profile is done. We have also studied the variation of pulse profile and pulse fraction with energy using *NuSTAR* observation. The pulse-phase, orbital-phase and time resolved spectral analysis are also obtained.

4.2 Observation and data reduction

We have used one *NuSTAR* and three *Swift*-XRT observations of the source Swift J1756.9-2508 (hereafter J1756.9) for our analysis. Data reduction were performed in HEASOFT v 6.22.1. Out of the seven *Swift* observations the source was clearly visible in four cases. The observation IDs of the *Swift* observations used in our analysis are 00030952018, 00088662001, 00030952019 and 00030952020. The standard data screening and reduction of *Swift*-XRT data are done through *xrtpipeline* (v 0.13.4). The source and background region file are obtained using *xselect*. For the last three observations the count rates are found greater than 0.5 count s^{-1} and therefore, the pile up effect is not-negligible. So to minimize the pile-up effects we took an annular region of radius 3 and 23 pixels around the bright source center for all the observations as a source region, whereas the circular region of radius 20 pixel away from the source was considered as background region. The observation of the source was contaminated with the presence of bright source GX 5-1 in the close proximity, so the background region is so chosen that it includes the maximum contamination. The response matrix files are obtained from the calibration data base whereas the ancillary response files are generated using the tool *xrtmkarf*. During the 2018 outburst *NuSTAR* observed the source twice. The observations IDs are 90402313002 and 90402313004. The source was visible only during the first observation, it was in quiescent state however during the second observation. So we have considered the first *NuSTAR* observational data only for analysis. The standard data reduction along with the products

are obtained using *NuSTAR* data analysis software (*NuSTAR*DAS v 1.9.3). The clean event files from the unfiltered event files for the two focal plane modulus FPMA & B have been obtained using *nupipeline*. The image from the cleaned event files are plotted using *xselect* and *ds9*. From the plotted image the source region were extracted considering a circular radius of $90'$ around the direction of the source and the background region was obtained by taking a circular region of same radius away from the direction of the source. The light curves and spectra are then obtained using these sources and background regions with the help of *nuproducts*. The light curves from the two focal plane modulus were background corrected and combined using the tool *lcmath*. Finally the barycentric correction of the combined light curve was done with the help of the *barycorr* in the analysis.

4.3 Analysis and Results

4.3.1 Light curves

Light curves of the AMXP J1756.9 during 2018 outburst are shown in Fig. 4.1. The light curve in black is from *Swift*-BAT, whereas that in the red colour in the Fig. 4.1 is from *Swift*-XRT. The vertical dotted line represents the *NuSTAR* observation. The inset figure represents the AMXP light curve for a *NuSTAR* observation. From the *NuSTAR* light curve we observed that the count rate decreases quickly by $\sim 3.15 \text{ count s}^{-1}$ or by about 15% in 84.5 ks. Thus the count rate decreases at the rate of $\sim 3.22 \text{ count s}^{-1}$ per day. Fitting the *NuSTAR* light curve with a straight line determined the slope $\sim 3.63 \text{ count s}^{-1}$ per day, considering this to be the decay rate then after six days the count rate is then found to decrease by $\sim 22 \text{ count s}^{-1}$, that is why the source was undetectable during second *NuSTAR* observation. Thus the source was observed once again nearly six days after the first observation.

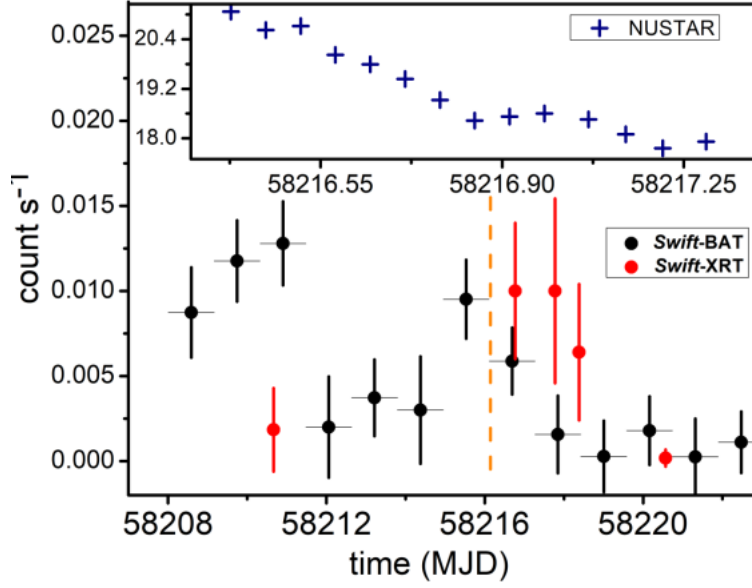


Fig. 4.1 Light curves of J1756.9 during 2018 outburst. Black and red represents the *Swift*-XRT & BAT light curves respectively. The inset figure represent *NuSTAR* light curve.

Colour-colour diagram

The colour-colour diagram gives the variation of the hard colour with respect to soft colour. The soft colour is obtained by dividing the light curve of 5-8 keV energy by light curve of 3-5 keV, whereas the hard colour is analyzed as the ratio of 8-14 keV to 14-22 keV count rates. The colour-colour diagram is found different during this outburst as compared to that reported by Patruno *et al.* (2010a) and it can be due to the fact that this particular *NuSTAR* observation covers only a fraction of the outburst. The soft and hard colours lies between 1.0-2.7 and 1.2-1.8 respectively. The soft colour is more prominent in 1.2-1.8 range corresponding to the hard colour in 0.25-0.40 range.

4.3.2 Pulse profiles

To get the pulse profile we estimated the pulse period of the AMXP. The pulse period was estimated using the ftool *efsearch* which uses χ^2 maximization technique. The estimated pulse period was about 5.4925 ms. Pulse profiles were obtained by folding the light curves

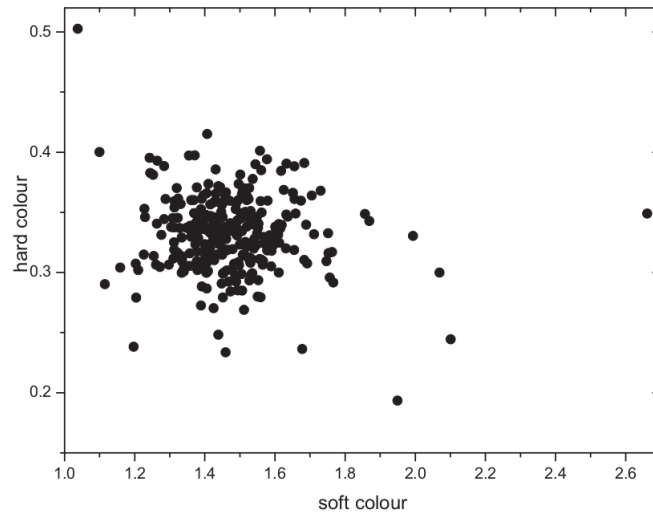


Fig. 4.2 Colour-colour diagram of the AMXP.

about the estimated pulse period using EFOLD. The pulse profiles were folded into 10 phase bins. The pulse profile in the energy range 3-79 keV of the J1756.9 is found to deviate from the sinusoidal shape as the second harmonic component has non-negligible contribution to the pulse profile as observed by Bult *et al.* (2018); Sanna *et al.* (2018). To understand more clearly about the contribution of first and second harmonic components we fitted the pulse profile by two sinusoidal functions (fundamental and second harmonics). The two sinusoidal fittings are represented by the blue (fundamental) and the red (second harmonic) colours in the Fig. 4.3, whereas the black represents the best fitted line.

The pulse profiles variation with the energy is studied by folding the light curves in four different energy ranges namely 3-7 keV, 7-17 keV, 17-35 keV and 35-79 keV, each having 10 phase bins. These pulse profiles were also fitted with two sinusoidal functions. The shape of the pulse profiles were observed to vary with the energy. A significant deviation of the pulse profiles from the sinusoidal shape is observed, which clear indicates about the contribution of the second harmonic component. For hard X-ray range the deviation is much stronger, as it is clear from the Fig. 4.3. For the pulse profiles in 17-35 keV and

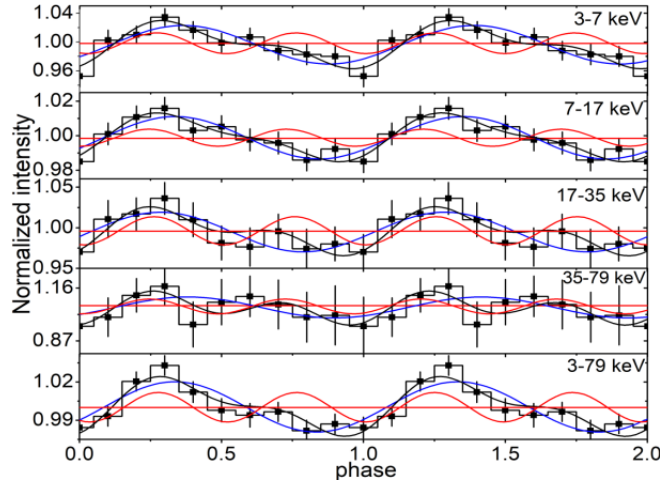


Fig. 4.3 Pulse profiles in five different energy range. The fundamental and second harmonic sinusoidal fitting are represented by blue and red respectively. The black line represents the best fitted line.

35-79 keV the deviation from the sinusoidal shape is much more than the other three cases. The pulse profile in 35-79 keV is found to have nearly double peak.

Patruno *et al.* (2010a) studied the variation of pulse profile with time during 2007 and 2009 outbursts of J1756.9, where it was shown that the pulse profiles were sinusoidal in shape at the beginning of the outburst. Then it gradually evolved into skewed shape during the slow decay phase of the outburst and thereafter became double peaked in the fast decay phase of the outburst. It is also important to note that the variation in the shape of the pulse profile is related with the variation of pulse amplitude and pulse phase with time. They also observed the same kind of variation in pulse profile with time during the two outbursts.

Pulse morphology

To understand in depth about the dependence of the pulse profiles with energy we used the procedure followed by Tendulkar *et al.* (2015). The idea behind this is to decompose the pulses into Fourier harmonics such that we define two Fourier co-efficient a_k and b_k as,

$$a_k = \frac{1}{N} \sum_{j=1}^N p_j \cos\left|\frac{2\pi jk}{N}\right| \quad (4.1)$$

$$b_k = \frac{1}{N} \sum_{j=1}^N p_j \sin \left| \frac{2\pi jk}{N} \right| \quad (4.2)$$

where N represents number of phase bins, j and k are the phase bins and Fourier harmonics respectively and p_j is the count rate of j^{th} phase bin. The strength of each of the Fourier component is defined as $A_k = \sqrt{a_k^2 + b_k^2}$, such that we can define another quantity A which is given by $A = \sqrt{\sum_{k=1}^M A_k^2}$. As the contribution of harmonics other than the second harmonic is negligible on the pulse profiles of AMXPs (Patruno and Watts, 2013) and also the Fourier co-efficient for higher harmonics are very small, so we consider upto first three harmonics in our analysis and therefore consider $M = 3$. In Fig. 4.4 the variation of the normalized amplitude of the fundamental A_1/A and second harmonics A_2/A are shown. For energy upto 40 keV, the normalized amplitude of the fundamental increases after that there is small decrease in its value at ~ 55 keV. The value of normalized amplitude of the second harmonics decreases upto 40 keV and then increases at last at ~ 55 keV. Fitting the normalized amplitudes of the fundamental and harmonics by straight line we observed that there is overall increase in the value of the normalized amplitude of the fundamental with energy whereas the normalized amplitude of the harmonic decreases with energy.

Pulse fraction

The strength of the pulsation is measured in terms of pulse fraction. Here we considered two different definitions of the pulse fraction found in the literature. The root-mean-square (rms) pulse fraction (P_{rms}) in terms of two Fourier coefficients is defined as follows:

$$PF_{rms} = \frac{\sqrt{2 \sum_{k=1}^M [(a_k^2 + b_k^2) - (\sigma_{a_k}^2 + \sigma_{b_k}^2)]}}{a_0} \quad (4.3)$$

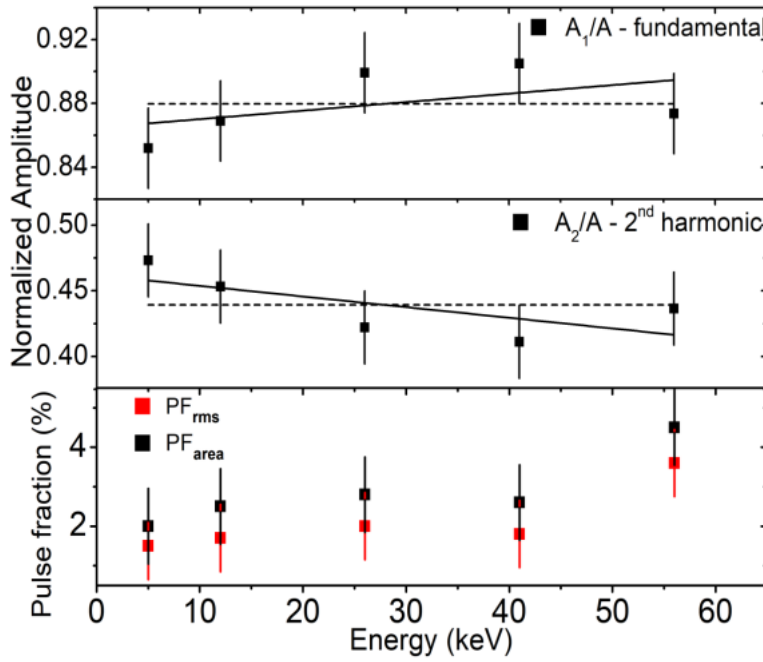


Fig. 4.4 Variation of normalized amplitude of first (upper panel) and second harmonic (middle panel) with energy. The bottom panel shows the variation of the pulse fraction with energy.

where a_k and b_k are the Fourier co-efficient as defined in equation 4.1 and 4.2. σ_{a_k} and σ_{b_k} are the uncertainties linked with a_k and b_k , where

$$\sigma_{a_k}^2 = \frac{1}{N} \sum_{j=1}^N \sigma_{p_j}^2 \cos^2 \left| \frac{2\pi jk}{N} \right| \quad (4.4)$$

$$\sigma_{b_k}^2 = \frac{1}{N} \sum_{j=1}^N \sigma_{p_j}^2 \sin^2 \left| \frac{2\pi jk}{N} \right| \quad (4.5)$$

Another definition of the pulse fraction is as follows (Gonzalez *et al.*, 2010):

$$PF_{area} = \frac{\sum_{j=1}^N (p_j - p_{min})}{\sum_{j=1}^N p_j} \quad (4.6)$$

The variation of the pulse fraction with the energy is plotted in the bottom panel of Fig. 4.4. It is observed that both the pulse fractions increases with the increase in energy.

$n_H (\times 10^{22})$	$8.64 \pm 0.49 \text{ cm}^{-2}$
kT	0.53 ± 0.02
photon index (α)	1.75 ± 0.02
cutoff energy (E_c)	74.58 ± 6.04
χ^2/dof	0.99/4731

Table 4.1 The best fitted model parameters obtained by fitting *Swift* and *NuSTAR* spectra simultaneously.

In 5-26 keV energy range both PF_{rms} and PF_{area} are found to increase slowly with the energy and a small decrease in their values at ~ 42 keV are observed followed by an abrupt increase in their value at 55 keV. However the variation of PF_{area} with energy is found to be steeper than that of the PF_{rms} . This can be due to the fact that the high energy X-ray photons are less in number than the soft X-ray photons, so PF_{area} is found to be biased towards the higher value due to the low statistics in the high energy range (An *et al.*, 2015).

4.3.3 Spectral analysis

A broadband spectral fitting in the energy range 0.3-79.0 was done by fitting simultaneously one of the *Swift*-XRT spectrum in 0.3-10 keV energy range with the 3-79 keV *NuSTAR* spectra. This particular *Swift* observation having Obs ID. 00088662001 was close to the first *NuSTAR* observation. Spectral fittings were done in XSPEC v12.9.1p. The models used in the analysis are CONSTANT, WABS, BLACKBODY and CUTOFFPL. The CONSTANT model is introduced in order to address the issue of the uncertainty of the instrumental calibrations and non-simultaneity of the *Swift* and *NuSTAR* observations.

The column density estimated by the model was about $\sim 8.64 \times 10^{22} \text{ cm}^{-2}$ which is much higher than that of expected value of $\sim 1 \times 10^{22} \text{ cm}^{-2}$ along the direction of the source. The broad 0.3-79 keV energy spectrum was observed to be hard and flat with a high value of cut-off energy 74.58 keV. The source is highly obscured which is indicated by the large absorption column density along the direction of the source. No emission or

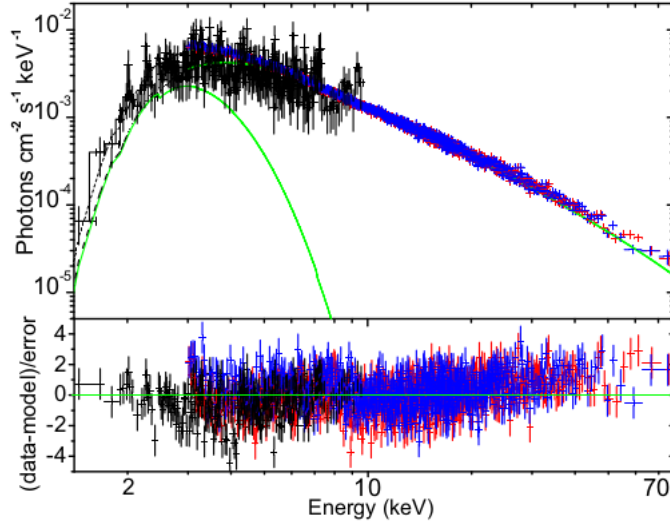


Fig. 4.5 The broad 0.3-79 keV spectral fitting of J1756.9. The points in black represents *Swift*-XRT spectrum and that one blue and red represent *NuSTAR* FPMA & B spectra respectively.

absorption like features were observed in the spectrum. The flux in 0.3-79.0 keV range is found to be $6.48 \times 10^{-10} \text{ erg cm}^{-2} \text{ s}^{-1}$. Considering the distance to the source to be 8 kpc (Krimm *et al.*, 2007b) the luminosity is found to be $4.96 \times 10^{36} \text{ erg s}^{-1}$. The best fitted parameters are shown in Table 4.1.

Pulse phase-resolved spectral analysis

Using *NuSTAR* observation of the J1756.9 we carried out the pulse phase-resolved analysis. For that we took a 5 ks long data segment and divided it into five equal pulse phase interval namely 0.0-0.2, 0.2-0.4, 0.4-0.6, 0.6-0.8 and 0.8-1.0 using the estimated value of pulse period. The necessary good time interval *gti* file for each phase interval was created in *xselect*. Using this *gti* file spectra for each interval are created with the help of *nuproducts*. The 3-79 keV spectra are then analyzed with CONSTANT, WABS and POWERLAW models. The flux is estimated using the model CFLUX. The CONSTANT model parameters were fixed at unity. It is observed that the photon index is maximum in the initial phase interval 0.0-0.2 which decreases in the next phase interval reaching a

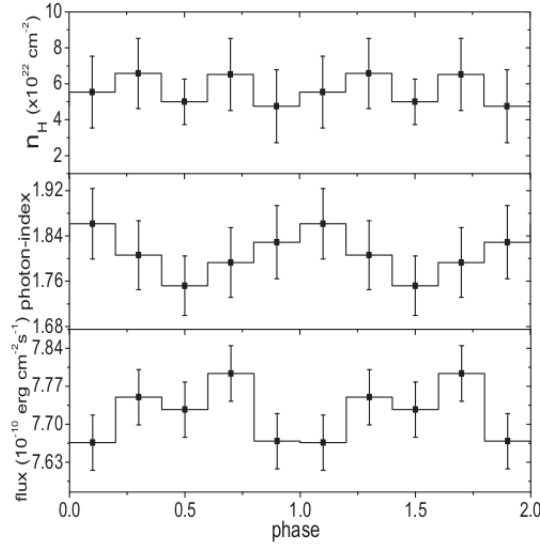


Fig. 4.6 Variation of the spectral parameter with the pulse phase. The upper, middle and bottom panels shows variation of column density (n_H), photon index and flux with the pulse phase respectively.

phase ϕ	n_H cm^{-2}	Photon index α	Flux (\times) $ergcm^{-2}s^{-1}$	χ^2_v
0.0-0.2	5.53 ± 1.99	1.86 ± 0.06	7.666 ± 0.051	0.89
0.2-0.4	6.57 ± 1.95	1.80 ± 0.06	7.750 ± 0.050	0.92
0.4-0.6	4.99 ± 1.26	1.75 ± 0.06	7.727 ± 0.049	0.94
0.6-0.8	6.52 ± 2.01	1.79 ± 0.06	7.794 ± 0.051	0.94
0.8-1.0	4.75 ± 2.03	1.83 ± 0.06	7.669 ± 0.050	0.97

Table 4.2 Values of best fitted spectral parameters.

minimum at 0.4-0.6 and then increases once again in the rest of the phase intervals. No systematic variation of the column density with the pulse phase were observed. The flux is observed to decrease with the phase and it reaches the maximum value in the interval 0.6-0.8 after that it decreases as depicted in Fig. 4.6. The best fitted model parameters are estimated which are displayed in the Table 4.2.

Orbital phase resolved analysis

For orbital phase analysis we used the value of orbital period and epoch obtained by Sanna *et al.* (2018). Using *NuSTAR* observation we divided the total orbital period into ten phase

intervals. For each interval good time interval (*gti*) file was created. Using this good time interval we extracted the spectra for each of the orbital phase interval. Spectra were fitted with CONSTANT, WABS and POWERLAW models. The flux in 3-79 keV energy range was estimated using the convolution model CFLUX. The variation of the spectral parameter with the orbital phase is shown in Fig. 4.7.

It is observed that between the phase interval 0.0-0.2 the flux increases and then it decreases which is followed by an increase and thereafter decrease and once again it increases reaching a maximum value of $5.99 \times 10^{-10} \text{ erg cm}^{-2} \text{ s}^{-1}$ in between 0.5-0.6. After that it is found that the flux decreases continuously between 0.6-0.9, reaching the minimum value of $5.56 \times 10^{-10} \text{ erg cm}^{-2} \text{ s}^{-1}$ and then increase once again in the last phase interval 0.9-1.0. The photon index decreases regularly in between 0.0-0.5 and then increases in the phase interval 0.5-0.7. After that there is a decrease in its value which is followed by an increase and then small decrease in its value. The column density is found to vary similarly with the orbital phase as the photon index. In between 0.0-0.3 the value of column density decreases after that there is a sharp rise and fall. In the interval 0.4-0.7 the value of column density increases which is followed by a decrease and an increase in the values. In between the phase interval 0.8-1.0 the value of column density is almost constant. The cutoff energy decreases between the orbital phase 0.0-0.5 and then increases sharply in 0.5-0.6 phase interval followed by a small increase in its value at 0.6-0.7. After that there is a sharp fall in its value followed by sharp rise. For 0.8-1.0 the value of cutoff energy is almost constant. The value of different spectral parameters are shown in Table 4.3.

The correlation of different spectral parameters with flux is also studied here. For that we have plotted the photon index, column density and cutoff energy against the flux. This is shown in Fig. 4.8. From the figure it is evident that the column density and photon

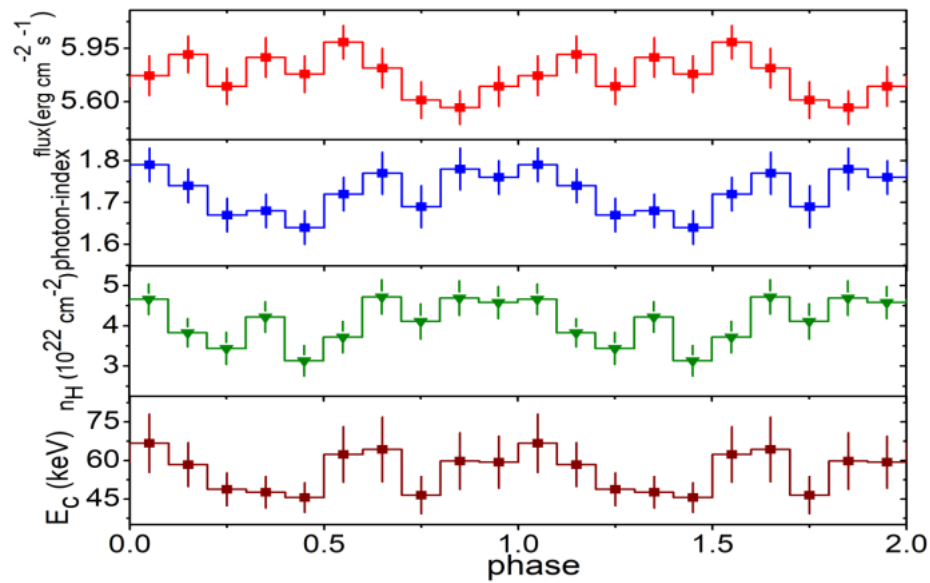


Fig. 4.7 Variation of the best fitted spectral parameter with the orbital phase. The upper panel in red shows the variation of flux with phase. The figures in blue and green indicated the variation of photon index and column density respectively. The lower panel shows the variation of cutoff energy with phase.

index show anti-correlation with the flux whereas the cutoff energy (E_c) shows a positive correlation with both flux and photon index.

Time resolved spectral analysis

To study the variation of the spectrum with time we divided the total exposure time of 39.5 ks into 14 segments. The mean exposure time of each segment being ~ 2.8 ks. For each segment good time interval file created. Using this good time interval file spectra were extracted. Spectra were fitted with the same model as have been used earlier to fit the spectra. The variation of the spectral parameters with the time is shown in Fig. 4.9. From the figure it is evident that the flux is found to decrease with time which is clear from the plot that the outburst is decaying rapidly. However there is no monotonous decrease or increase in the spectral parameters with time. The spectral parameter shows increase and decrease with time. An abrupt increase in the spectral parameters at the last interval is observed. Using GAUSSIAN model we searched for the iron line, first we kept the

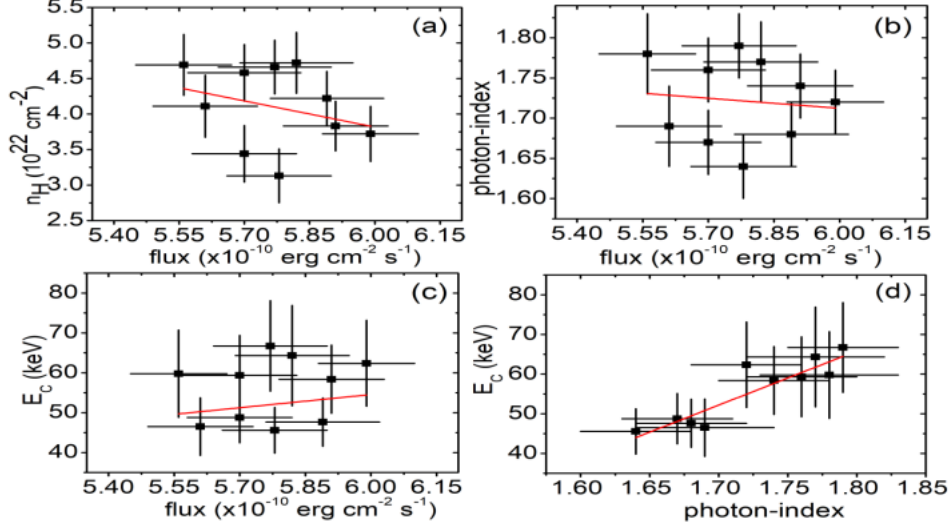


Fig. 4.8 Variation of the column density (a), photon index (b) and cutoff energy (c) with flux. Variation of cutoff energy (d) with photon index.

Phase	n_H (10^{22} cm^{-2})	Photon index α	E_c (keV)	Flux ($10^{-10} \text{ erg cm}^{-2} \text{ s}^{-1}$)	χ^2_ν
0.0-0.1	4.7 ± 0.4	1.79 ± 0.04	66.7 ± 11.4	5.77 ± 0.13	0.97
0.1-0.2	3.8 ± 0.3	1.74 ± 0.04	58.4 ± 8.6	5.91 ± 0.12	0.91
0.2-0.3	3.4 ± 0.4	1.67 ± 0.04	48.8 ± 6.4	5.70 ± 0.12	0.91
0.3-0.4	4.2 ± 0.4	1.68 ± 0.04	47.6 ± 6.1	5.89 ± 0.13	0.88
0.4-0.5	3.1 ± 0.4	1.64 ± 0.04	45.6 ± 5.8	5.78 ± 0.12	0.86
0.5-0.6	3.7 ± 0.4	1.67 ± 0.04	62.4 ± 10.8	5.99 ± 0.11	0.87
0.6-0.7	4.7 ± 0.4	1.77 ± 0.05	64.3 ± 12.6	5.82 ± 0.13	0.83
0.7-0.8	4.1 ± 0.4	1.69 ± 0.05	46.5 ± 7.2	5.61 ± 0.12	0.90
0.8-0.9	4.7 ± 0.4	1.78 ± 0.05	59.8 ± 11.0	5.56 ± 0.11	0.85
0.9-1.0	4.6 ± 0.4	1.76 ± 0.04	59.3 ± 10.1	5.70 ± 0.13	0.90

Table 4.3 Best fitted spectral parameters for different orbital phase intervals.

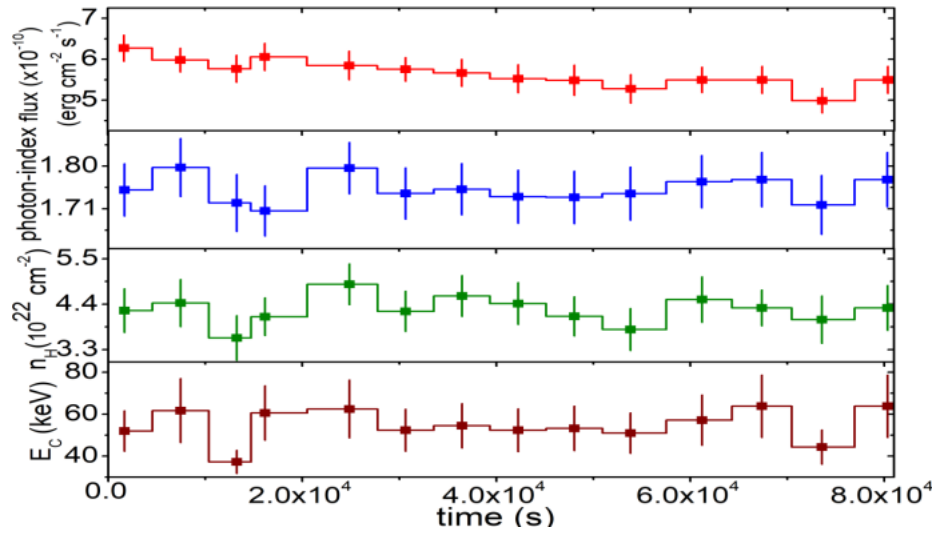


Fig. 4.9 The first upper panel in red indicates the variation of flux with time. The bottom panel indicates the variation of cutoff energy with the time. The two middle panels in blue & green represent the variation of photon index and the column density with time respectively.

Gaussian line fixed at 6.4 keV and then fitted it, after that we set the Gaussian line free and fitted the spectra again. However no iron emission lines are observed. The upcoming mission with high spectral resolution is helpful in finding the presence of iron line in J1756.9 and other AMXPs. No spectral softening or hardening of the spectrum with time is observed. From the Fig. 4.9 it is evident that a correlation is observed between the photon index (α), column density (n_H) and cutoff energy (E_c) as in some part of the figure these parameters follows the same pattern. To check this correlation we have plotted the these parameters with respect to the spectral flux (Fig. 4.10). When the variation is fitted with a linear model we found a straight line having non-zero positive slope, which indicates the existence of correlation. The correlation can be understood in the way that with the generation of high energy X-ray photons there is an increase in their absorption resulting in an increase in column density and softening of spectrum however sufficient number of high energy photons which can still reach the detector. Table 4.4 gives the detail variation of the spectral parameter with time.

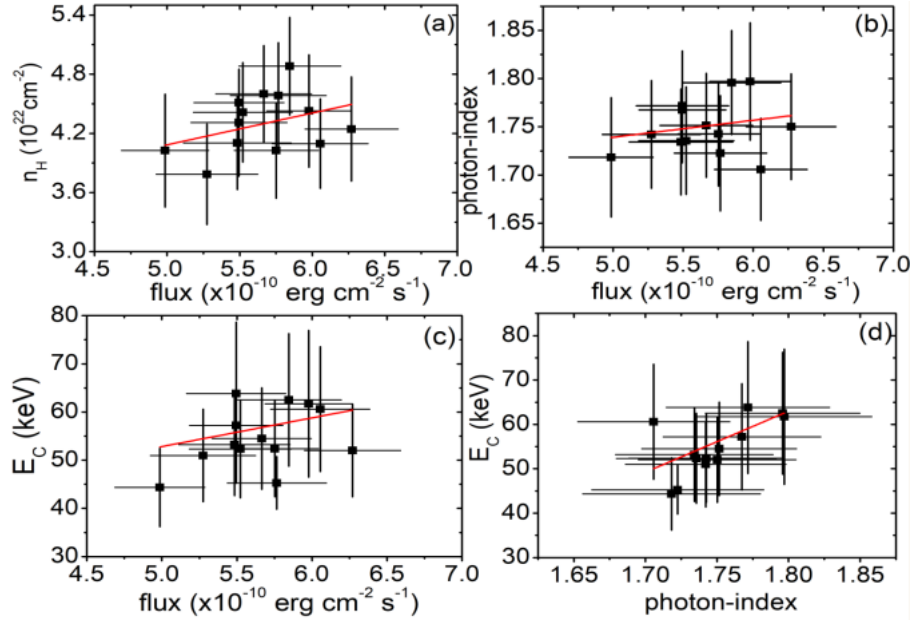


Fig. 4.10 Figures (a), (b) and (c) represents variation of column density, photon index and cutoff energy with flux respectively, whereas that in figure in panel (d) is variation of cutoff energy with the photon index.

Time (ks)	n_H (10^{22} cm^{-2})	Photon index (α)	E_c (keV)	Flux ($10^{-10} \text{ erg cm}^{-2} \text{ s}^{-1}$)	χ^2_ν
0-3.3	4.2 ± 0.5	1.70 ± 0.06	52.0 ± 9.6	6.27 ± 0.32	0.87
6-9	4.4 ± 0.6	1.80 ± 0.06	61.7 ± 15.2	5.98 ± 0.29	0.86
12-15	3.6 ± 0.5	1.63 ± 0.06	37.3 ± 5.5	5.76 ± 0.33	0.90
17-21	4.1 ± 0.4	1.74 ± 0.05	60.6 ± 12.9	6.05 ± 0.33	0.86
23-26	4.9 ± 0.5	1.79 ± 0.05	62.5 ± 13.7	5.84 ± 0.35	0.78
29-32	4.2 ± 0.5	1.74 ± 0.05	52.4 ± 10.0	5.75 ± 0.29	0.90
35-38	4.6 ± 0.5	1.75 ± 0.05	54.5 ± 10.5	5.66 ± 0.33	0.85
41-44	4.4 ± 0.5	1.74 ± 0.06	52.3 ± 10.2	5.52 ± 0.34	0.91
46-50	4.1 ± 0.5	1.73 ± 0.06	53.2 ± 10.6	5.48 ± 0.37	0.86
52-55	3.8 ± 0.5	1.74 ± 0.06	51.0 ± 9.6	5.27 ± 0.35	0.81
58-63	4.5 ± 0.6	1.77 ± 0.06	57.2 ± 12.0	5.49 ± 0.31	0.88
65-70	4.3 ± 0.4	1.77 ± 0.06	63.8 ± 14.9	5.49 ± 0.33	0.78
71-76	4.0 ± 0.6	1.72 ± 0.06	44.3 ± 8.2	4.99 ± 0.30	0.97
76-84	4.3 ± 0.5	1.77 ± 0.06	63.8 ± 14.9	5.49 ± 0.33	0.78

Table 4.4 Table showing the variation of the best fitted spectral parameters with time.

Obs ID	Date of obs (MJD)	n_H (10^{22}cm^{-2})	Photon index (α)	Flux ($\times 10^{-11} \text{ergcm}^{-2} \text{s}^{-1}$)	χ^2_ν
00030952018	58210.67	6.55 ± 2.85	1.52 ± 0.64	13.93	0.85
00088662001	58216.77	6.06 ± 0.59	1.75 ± 0.18	14.96	0.76
00030952019	58217.78	7.99 ± 1.07	2.31 ± 0.30	10.82	0.71
00030952020	58218.38	4.08 ± 1.35	0.94 ± 0.47	6.67	0.73

Table 4.5 The best fitted spectral parameter for different *Swift*-XRT observation.

The *Swift*-XRT spectra in 0.3-10.0 keV were also fitted by a simple POWERLAW model. The best fitted spectral parameter for different observations are shown in Table 4.5 along with their observation IDs. In between 58210.67 and 58217.78 the photon index increases from 1.52 to 2.31 MJD and after that it decreases to 0.94. The flux was observed to increase between 58210.67 and then decreases. So softening of spectrum with an increase in flux is observed as we have observed in the time resolved spectral analysis of the AMXP using *NuSTAR* observation.

4.4 Discussion

From the *NuSTAR* light curve of the AMXP it is clear that the outburst decays very rapidly. In 84.5 ks observation there was about $\sim 15\%$ decrease in the count rate. We presented the detail study of the change in the morphology of the pulse profile with the energy. As we have observed that the 3-79 keV pulse profile of the AMXP shows significant deviation from the sinusoidal shape, which possibly indicates the significant contribution of second harmonics on the pulse profile. It is evident that there was a change in the morphology of the pulse profile with the energy. The pulse profiles in 3-7 keV, 7-17 keV and 17-35 keV are non sinusoidal, whereas in the 35-79 keV pulse profile we found existence of double peak. The deviation are clearly shown by the black line in Fig. 4.3, which corresponds to best fitted line of the two harmonic components.

We have calculated the normalized amplitude of the first and second harmonics in terms Fourier components in the different energy bands. It is observed that the normalized amplitude of the first harmonic increases with energy and for the second harmonic it decreases with the energy. Similar types of variation in the fractional amplitudes of the Swift J1756.9-2508 was observed by Patruno *et al.* (2010a) using RXTE observations and Sanna *et al.* (2018) using *NuSTAR* and XMM-Newton observations. Bult *et al.* (2018) also reported similar variation of the normalized amplitudes with the energy. The variation of pulse profiles and fractional amplitude are observed in all AMXPs, for example the fractional amplitude in case of Aql X-1 (Casella *et al.*, 2008), SAX J1748.9-202 (Patruno *et al.*, 2010b) and IGR J17379-3747 (Bult *et al.*, 2019) increases with the energy. However in some AMXPs decrease in the fractional amplitude with energy is observed as in the case of XTE J0929-314 (Galloway *et al.*, 2007) and HETE J1900.1-2455 (Galloway *et al.*, 2007). In some cases AMXPs show complex variation in fractional amplitude with the energy, where both increase and decrease in its value are observed at different energies (see Patruno *et al.* (2010b); Falanga *et al.* (2005)). The dependence of the pulse fraction of pulse profile on the energy is studied here and found it increases with the energy. The increase in the pulse fraction with the energy can be understand by a simple toy model suggest by Alexander and Sergey (2008). It was interpreted by them that X-ray emitting region becomes smaller and smaller with the increase in energy and hence the X-rays becomes more pulsed. Patruno and Watts (2013) gave similar explanation to explain the observed variation of fractional amplitude of AMXPs with the energy. It was reported that with an increase in energy the amplitude of pulsed blackbody radiation emitted from the hot spots also increases. We have not observed aperiodic signal or broadband noise at ~ 0.1 Hz in the power spectrum of the AMXP as observed by Linares *et al.* (2008).

From broadband 0.3-79.0 keV spectral fitting of *Swift* and *NuSTAR* spectra we observed that the spectrum of Swift J1756.9-2508 was hard and flat having cutoff energy about

74.58 keV, which can be due to Comptonization of soft photons. Sanna *et al.* (2018) also observed the spectra of J1756.9 in hard state with high energy cutoff during the outburst. We have studied both pulse, orbital phase and time resolved spectral analysis. The photon index obtained by fitting the pulse phase resolved spectra of the J1756.9 by POWERLAW model shows the variation of photon index with pulse phase. The photon index decreases in the initial phases (0.0-0.6) and then increases in the rest of the pulse phases. The flux increase in between 0.0-0.8 except at 0.4-0.6 where we observed small decrease in flux (Fig. 4.6) and decreases abruptly at the last phase intervals. However no systematic variation in the photo-electric absorption in the phase is observed. The flux is minimum when the photon index is maximum; this can be as a result of absorption of X-rays during these phases. It can also be due to variation of the optical depth at different viewing angles which accounts for the variation of the flux and the photon index with pulse phase. The variation of spectral parameter with the pulse phase indicates presence of anisotropy in the accretion columns above the hotspots.

With the orbital phase the photon index (α) and column density (n_H) varies in the similar way but it shows anti-correlation with the source flux, however the cutoff energy (E_c) varies differently with orbital phase and flux. It is clear from Fig. 4.8 that n_H and α decreases with an increase in flux. Thus as a result of increase in flux the spectrum becomes more hard. The hardening of the spectrum with the flux can be as a result of an increase in the optical depth with an increase in the flux or mass accretion rate at the different orbital phases. There is no indication of hardening or softening of the spectrum with the time as observed from the time resolved spectral analysis, but the softening of the spectrum with the increase in flux is observed as the photon index increases with an increase in flux. Also the other spectral parameters obtained in the time resolved spectral analysis shows positive correlation with the flux. From the *Swift*-XRT spectral analysis too we observed that the photon index decreases with decrease in flux. This softening of

spectrum with an increase in the flux was also observed by Zhang *et al.* (1998) in Aql X-1. It was suggested that this might be the indication of source entering into propeller phase. The cutoff energy (E_s) shows positive correlation with flux in both the orbital and the phase resolved spectral analyses. The cutoff energy is associated with the temperature of plasma of the X-ray emitting region and in this case an increase in the observed flux indicates an increase in plasma temperature (Soong *et al.*, 1990). Hence an increase in flux results in an increase in cutoff energy E_c .

Sanna *et al.* (2018) also not observed any emission lines in the source spectra. Patruno *et al.* (2010a) observed the presence of emission line like feature in 6-7 keV energy range as a result it was unable to constraint its line energy and width, as the spectral resolution of the RXTE-PCA is very poor. However, Sanna *et al.* (2018) constraint the upper limit of the width of undetected iron line to be 5 eV. We did not observed any emission or absorption like features in the spectra of J1756.9.